A numerical study of the effect of particle properties on the radial distribution of suspensions in pipe flow

A. Pazouki[a,*], D. Negrut[a]

[a]*Department of Mechanical Engineering, University of Wisconsin-Madison, Madison, WI 53706-1572, USA*

Abstract

We employ a Lagrangian-Lagrangian (LL) numerical formalism to study two- and three-dimensional (2D, 3D) pipe flow of dilute suspensions of macroscopic neutrally buoyant rigid bodies at flow regimes with Reynolds numbers (Re) between 0.1 and 1400. A validation study of particle migration over a wide spectrum of Re and average volumetric concentrations demonstrates the good predictive attributes of the LL approach adopted herein. Using a scalable parallel implementation of the approach, 3D direct numerical simulation is used to show that (1) rigid body rotation affects the behavior of a particle laden flow; (2) an increase in neutrally buoyant particle size decreases radial migration; (3) a decrease in inter-particle distance slows down the migration and shifts the stable position further away from the channel axis; (4) rigid body shape influences the stable radial distribution of particles; (5) particle migration is influenced, both quantitatively and qualitatively, by the Reynolds number; and (6) the stable radial particle concentration distribution is affected by the initial concentration. The parallel LL simulation

*Corresponding author

Email addresses: pazouki@wisc.edu (A. Pazouki), negrut@wisc.edu (D. Negrut)

framework developed herein does not impose restrictions on the shape or size of the rigid bodies and was used to simulate 3D flows of dense, colloidal suspensions of up to 23,000 neutrally buoyant ellipsoids.

Keywords:
Pipe flow, particle radial migration, direct numerical simulation, fluid-solid interaction, Lagrangian-Lagrangian approach, Smoothed Particle Hydrodynamics

---

1. Introduction

The topic of particle migration has been of great interest since Segre and Silberberg experimentally investigated the pipe flow of a dilute suspension of spherical particles and demonstrated that, at a pipe Reynolds number (Re) between 2 and 700, the particles settle on an annulus with an approximate relative radius of 0.6 with respect to the pipe radius [64, 65]. Subsequent experiments conducted by Oliver [53], Jeffrey and Pearson [32], and Karnis *et al.* [34] confirmed and further investigated the particle radial migration. For dilute suspensions, Matas *et al.* [42] showed experimentally that the radius of stable annulus increases directly with Re. At a high Reynolds number, Re>650, they observed the formation of an inner annulus of smaller radius that had not been predicted analytically or observed through simulation. Moreover, they showed that the probability of a particle settling on this annulus of smaller radius increases with the Reynolds number. From an analytical perspective, perturbation methods have been widely employed to investigate the lift force responsible for particle migration, see for instance Saffman [61], Ho and Leal [26], Vasseur and Cox [71], Schonberg and Hinch

[63], Hogg [28], Asmolov *et al.* [2], and Matas *et al.* [43]. Particle migration has also been investigated in a number of numerical simulation studies. Feng *et al.* [19] employed a Finite Element Method (FEM) to study the migration of a single circular cylinder in plane Poiseuille flow. Inamuro et al. [31] investigated a similar problem using a Lattice Boltzmann Method (LBM). Chun and Ladd employed LBM to investigate the migration of spheres in a square duct at $Re<1000$ [11]. They showed that the stable lateral position of a single particle moves closer to the duct wall as the Reynolds number increases. For flows containing several particles, a first stable particle configuration forms at $Re<300$; a secondary stable region nearer to the center of the duct is observed at $Re>700$. Pan and Glowinski developed the method of Distributed Lagrange Multiplier/Fictitious Domain Method (DLM/FDM) in conjunction with a finite difference approach to investigate the shear induced migration of a circular cylinder [22] and a collection of spheres [57]. Shao *et al.* [66] investigated the motion of spheres in steady Poiseuille flow at moderately high Re using DLM/FDM. Their work confirmed the development of an inner stable annulus at high Re, i.e., $Re \geq 640$ for specific size and channel length ratio. Yu *et al.* [73] investigated the sphere sedimentation as well as the migration of a sphere in Poiseuille flow at $Re<400$ via the DLM method. Hu [30] and Hu *et al.* [29] employed the Arbitrary Lagrangian-Eulerian (ALE) method on a body-fitted unstructured finite element grid to simulate fluid-solid systems. Their work influenced that of Patankar *et al.* [58, 59] and Choi and Josef [9] in their study of the lift-off of cylinders in plane Poiseuille flow. Similar techniques have been considered to study the behavior of a non-spherical particle, usually an ellipsoid in fluid flow. Swami-

nathan *et al.* [69] used ALE based FEM to simulate the sedimentation of an ellipsoid. Pan *et al.* [54] investigated the motion of ellipsoid in Poiseuille flow using DLM/FDM. In several other studies the investigation of flows containing a collection of cylinders (2D) [8, 20, 67] and spheres (3D) [11, 29] was carried out via direct numerical simulation with the LBM [11, 20], Lagrange multiplier based fictitious domain method [8, 56, 67], and ALE-based FEM [29].

All these numerical studies of particle suspension and migration draw on an Eulerian-Lagrangian representation of the fluid-solid system. In this contribution, we employ a Lagrangian-Lagrangian (LL) approach to study the particle migration over a wide range of Reynolds numbers. The Smoothed Particle Hydrodynamics (SPH) method [21, 41] is relied upon for the fluid flow simulation. The SPH method is extensively reviewed in Monaghan [47] and Liu and Liu [40]. Herein, the Navier-Stokes equations, solved within the SPH framework, are coupled with Newton's equations of motion for rigid body dynamics to investigate, in a unitary framework, flows that include rigid bodies of arbitrary geometries. We used and validated the coupling algorithm reported in [60]. The possible solid to solid contacts, if any, are resolved via a lubrication force model [39].

The document is organized as follows: section 2 provides an overview of the numerical solution and its parallel implementation. Section 3 presents a set of validations of the proposed approach in relation to experiments that involve particle migration and distribution at $1<Re<1400$. The distribution validation exhibits more complexity than capturing only the stable radial position since attention must be paid to the rate of migration to the stable

configuration. In section 4, we report results of several parametric studies that investigate the effect of particle shape, size, distance, and concentration on particle radial migration. A scaling analysis carried out for a dense colloidal suspension of ellipsoids concludes the numerical experiment section.

2. Fluid-solid interaction simulation methodology

The SPH-based approach used herein to represent the dynamics of fluid flow accounts for the two-way coupling with rigid body dynamics by regarding body geometries as moving boundaries. The 3D rigid body rotation is characterized by means of a set of four Euler parameters [25]. In terms of notation, the term "marker" is employed to denote the SPH discretization point and "particle" to refer to a 3D rigid body, although the latter has geometry and experiences 3D rotation during its time evolution.

2.1. The Smoothed Particle Hydrodynamics method

An in-depth discussion of the SPH method and recent developments can be found in [40, 44, 47]. Herein, we highlight the essential components required to express the fluid-solid coupling.

SPH is a Lagrangian method that probes the fluid domain at a set of moving markers. Each marker has an associated kernel function with compact support that defines its domain of influence, as shown in Figure 1. The choice of kernel function W is not unique. A cubic spline interpolation kernel [48] was used in this work. At a point located by a position vector $\mathbf{r}$ with

respect to an SPH marker, the cubic spline interpolation kernel is defined as

$$W(q,h) = \frac{1}{4\pi h^3} \times \begin{cases} (2-q)^3 - 4(1-q)^3, & 0 \le q < 1 \\ (2-q)^3, & 1 \le q < 2 \\ 0, & q \ge 2 \end{cases}, \tag{1}$$

where h is the kernel function's characteristic length and $q \equiv |\mathbf{r}|/h$. The radius of the support domain, κh, is proportional to the characteristic length h through the parameter κ which is equal to 2 in the kernel function defined by Eq. (1). Although, a constant h was considered herein, using a variable h may be beneficial in some applications such as wave propagation in compressible flow [47].

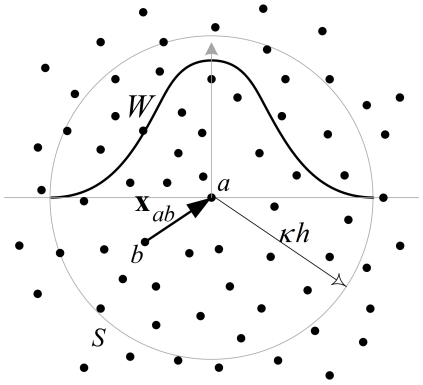

Figure 1: Illustration of the kernel, W, and support domain, S – shown for marker a. For 2D problems the support domain is a circle, while for 3D problems it is a sphere. SPH markers are shown as black dots.

The cubic spline kernel given in Eq. (1) is the most common smoothing kernel in one, two, and three dimensions owing to its reduced computational burden – a consequence of the small number of neighboring SPH markers typically required by the approach. Other researchers suggested that a smoother

second order derivative of the interpolation kernel can improve the SPH stability [40, 51, 70]. In [50] it was shown that the dispersion relation for linear waves can be undesirable for cubic splines with $\kappa = 2$. However, depending on the application, the artifacts can be negligible. Kernels that approximate the Gaussian function; i.e., higher order splines such as quartic ($\kappa = 2.5$) and quintic ($\kappa = 3$), have been shown to produce better results at the expense of a higher computational burden [51]. Similarly, Colagrossi and Landrini [12] tested third and fifth order B-splines as well as cut-normalized Gaussian kernels ($\kappa = 3$), and recommended the latter.

Using the SPH framework, the continuity and momentum equations, given respectively by

$$\frac{d\rho}{dt} = -\rho \nabla \cdot \mathbf{v} \ , \tag{2}$$

and

$$\frac{d\mathbf{v}}{dt} = -\frac{1}{\rho}\nabla p + \frac{\mu}{\rho}\nabla^2 \mathbf{v} + \mathbf{f} \ , \tag{3}$$

are discretized as [49]

$$\frac{d\rho_a}{dt} = \rho_a \sum_b \frac{m_b}{\rho_b} \left(\mathbf{v}_a - \mathbf{v}_b\right) \cdot \nabla_a W_{ab} \ , \tag{4}$$

and

$$\frac{d\mathbf{v}_a}{dt} = -\sum_b m_b \left((\frac{p_a}{{\rho_a}^2} + \frac{p_b}{{\rho_b}^2}) \nabla_a W_{ab} + \Pi_{ab} \right) + \mathbf{f}_a \ . \tag{5}$$

In Eq. (5), indices a and b denote the SPH markers, as shown in Figure 1, and

$$\Pi_{ab} = -\frac{(\mu_a + \mu_b)\mathbf{x}_{ab} \cdot \nabla_a W_{ab}}{\bar{\rho}_{ab}^2 (x_{ab}^2 + \varepsilon \bar{h}_{ab}^2)} \mathbf{v}_{ab} \tag{6}$$

imposes the viscous force based on the discretization of the ∇^2 operator. In terms of notation, ρ and μ are the fluid density and viscosity, respectively; $\mathbf{v}$ and p are flow velocity and pressure, respectively; m is the mass associated with an SPH marker; $\mathbf{f}$ is the volumetric force; t is the real time; $\mathbf{x}_{ab}$ is the relative distance between markers a and b, i.e. $\mathbf{x}_{ab} = \mathbf{x}_a - \mathbf{x}_b$; $W_{ab} \equiv W|_{\mathbf{r}=\mathbf{x}_{ab}}$; ∇_a is gradient with respect to $\mathbf{x}_a$, i.e. $\partial/\partial\mathbf{x}_a$; quantities with over-bar are the average of the same quantities for markers a and b; ε is a regularization coefficient, and the summation is over all markers within the support domain of marker a. We have evaluated several definitions for the viscosity as well as discretization of ∇^2 [47, 49] in conjunction with the simulation of transient Poiseuille flow and concluded that Π_{ab} of Eq. (6) led to the most accurate results in the widest range of Reynolds numbers. Moreover, Eq. (6) replaces the tuning parameters used in artificial viscosity [47] with physics-based fluid viscosity. This results are in agreement with [4], where different viscosity discretization approaches for a low Reynolds number simulation of transient Poiseuille flow were investigated.

The pressure p is evaluated using an equation of state [5, 13, 47]

$$p = \frac{{c_s}^2 \rho_0}{\gamma} \left\{ \left(\frac{\rho}{\rho_0} \right)^{\gamma} - 1 \right\}, \tag{7}$$

where ρ_0 is the reference density of the fluid, γ tunes the stiffness of the pressure-density relationship and normally has the value $\gamma = 7$, and c_s is the speed of sound. In the weakly compressible SPH method, c_s is adjusted depending on the maximum speed of the flow, $V_{\max}$, to keep the flow compressibility below any arbitrary value. Monaghan suggested the use of $c_s = 10V_{\max}$ for a compressibility less than 1% [47]. The analysis leading to this conclusion neglects the numerical artifacts introduced by the particle ap-

proximation. In practice, we observed larger compressibility. By increasing the numerical value of c_s, e.g. up to $c_s = 50V_{\max}$, the flow incompressibility was improved at the expense of smaller integration time steps.

The fluid flow equations (4) and (5) are solved in conjunction with Eq. (8) to update the position of the SPH markers:

$$\frac{d\mathbf{x}_a}{dt} = \mathbf{v}_a. \tag{8}$$

Compared to Eq. (4), which evaluates the time derivative of the density, the original SPH summation formula calculates the density according to

$$\rho_a = \sum_b m_b W_{ab}. \tag{9}$$

Equation (4) was preferred to Eq. (9) since it produced a smooth density field and worked well for markers close to the boundaries, i.e., the free surface, solid, and wall. However, Eq. (4) does not guarantee consistency between a marker's density and associated mass and volume [6, 46, 49]. Using Eq. (9) has problems of its own, e.g., the density field can experience large variations, particularly close to the boundary. One of the approaches suggested to resolve this issue is to combine the two methods in a so-called "density re-initialization technique" [12] in which Eq. (4) is implemented at each time step while Eq. (9) corrects the mass-density inconsistency every n time steps. The results reported herein were obtained with $n = 10$. The Moving Least Squares method or a normalized version of Eq. (9) could alternatively be used to address the aforementioned issues [12, 15].

Finally, we employ the extended SPH approach, XSPH, which prevents extensive overlap of markers support domain and enhances incompressibility

of the flow [45]. This correction takes into account the velocity of neighboring markers through a mean velocity evaluated within the support of a nominal marker a as

$$\langle \mathbf{v}_a \rangle = \mathbf{v}_a + \Delta \mathbf{v}_a, \tag{10}$$

where

$$\Delta \mathbf{v}_a = \zeta \sum_b \frac{m_b}{\bar{\rho}_{ab}} (\mathbf{v}_b - \mathbf{v}_a) W_{ab}, \tag{11}$$

and $0 \leq \zeta \leq 1$ adjusts the contribution of the neighbors' velocities. All the results reported herein were obtained with $\zeta = 0.5$. The modified velocity calculated from Eq. (10) replaces the original velocity in the density and position update equations, but not in the momentum equation [12].

2.2. Rigid body dynamics

The dynamics of the rigid bodies is fully characterized by the Newton-Euler equations of motion, see for instance [25],

$$\frac{d\mathbf{V}_i}{dt} = \frac{\mathbf{F}_i}{M_i}, \tag{12}$$

$$\frac{d\mathbf{X}_i}{dt} = \mathbf{V}_i, \tag{13}$$

$$\frac{d\boldsymbol{\omega'}_i}{dt} = {\mathbf{J'}_i}^{-1} \left(\mathbf{T'}_i - \widetilde{\boldsymbol{\omega'}}_i \mathbf{J'}_i \boldsymbol{\omega'}_i \right), \tag{14}$$

$$\frac{d\mathbf{q}_i}{dt} = \frac{1}{2} {\mathbf{G}_i}^T \boldsymbol{\omega'}_i, \tag{15}$$

and

$${\mathbf{q}_i}^T \mathbf{q}_i - 1 = 0, \tag{16}$$

where $\mathbf{F}_i$, $\mathbf{T'}_i$, $\mathbf{X}_i$, $\mathbf{V}_i$, $\boldsymbol{\omega'}_i$, $\in \mathbb{R}^3$, denote the force, torque, position, velocity, and angular velocity associated to body i, respectively; $\mathbf{q}_i = \left[q_x^i,\, q_y^i,\, q_z^i,\, q_w^i\right]^T$, $\mathbf{J'}_i$ and M_i, are the rotation quaternion, moment of inertia, and mass, respectively; and $i \in \{1,\, 2,\, 3,\, ...,\, n_b\}$ is the rigid body index where n_b is the total number of rigid bodies in the system. Quantities with a prime symbol are represented in the rigid body local reference frame. Given $\boldsymbol{\omega'}_i = [\omega_x, \omega_y, \omega_z]^T$ and $\mathbf{q} = [q_x,\, q_y,\, q_z,\, q_w]^T$, the auxiliary matrices $\widetilde{\boldsymbol{\omega'}_i}$ and $\mathbf{G}$ are defined as [25]

$$\widetilde{\boldsymbol{\omega'}_i} = \begin{bmatrix} 0 & -\omega_z & \omega_y \\ \omega_z & 0 & -\omega_x \\ -\omega_y & \omega_x & 0 \end{bmatrix},\ \mathbf{G} = \begin{bmatrix} -q_y & q_x & q_w & -q_z \\ -q_z & -q_w & q_x & q_y \\ -q_w & q_z & -q_y & q_x \end{bmatrix}. \quad (17)$$

2.3. Fluid-solid interaction

The two-way fluid-solid coupling was implemented based on a methodology described in [60]. The state update of any SPH marker relies on the properties of its neighbors and resolves shear as well as normal inter-marker forces. For the SPH markers close to solid surfaces, the SPH summations presented in Eqs. (4), (5), (9), and (11) capture the contribution of fluid markers. The contribution of solid objects is calculated via Boundary Condition Enforcing (BCE) markers placed on and close to the solid's surface as shown in Figure 2. The velocity of a BCE marker is obtained from the rigid body motion of the solid and as such it ensures the no-slip condition on the solid surface. Including BCE markers in the SPH summation equations, i.e. Eqs. (4) and (5), results in fluid-solid interaction forces that are added to both fluid and solid markers.

Once the fluid-solid interaction between individual markers, i.e., the right hand side of Eqs. (4) and (5), is accounted for, the total rigid body force and

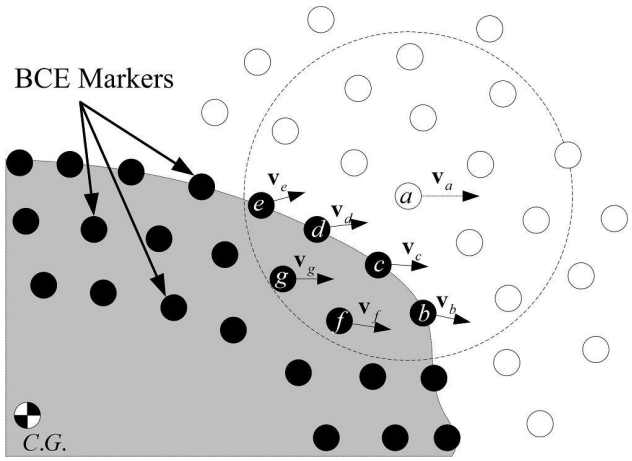

Figure 2: BCE and fluid markers, key for the coupling between fluid and solid, are represented by black and white circles, respectively. A section of the rigid body is shown herein as the gray area. The BCE markers positioned in the interior of the body (markers g and f in the figure) are placed at a depth less than or equal to the size of the compact support associated with the kernel function W.

torque due to the interaction with the fluid can be obtained by respectively summing the individual forces and their induced torques over the entire rigid body. They are then added to the other forces, including external and contact forces.

2.4. Short range interaction

Dry friction models, typically used to characterize the dynamics of granular materials [1, 36, 37], do not capture accurately the impact of solid surfaces in hydrodynamics media. In practice, it is infeasible to fully resolve the short-range, high-intensity forces associated with impact in wet media due to computational limits on space resolution and time step. By assuming smooth surfaces, Davis *et al.* followed the Hertz contact theory of linear

elasticity to calculate the pressure at the interface of two approaching elastic spheres in close proximity [14]. Their calculation showed that particles do not rebound at small Stokes number, $St = (2/9)(\rho_p/\rho)Re_p$, where ρ_p and Re_p are particle density and particle Reynolds number, respectively. The minimum St for a rebound after the hydroelastic impact depends on the spheres' rigidity. For rigid spheres, rebound happens at $St > 10$. An alternative approach to calculate the singular forces at contact relies on lubrication theory [17]. Ladd [39] proposed a normal lubrication force between two spheres that increases rapidly as the distance between spheres approaches zero thus preventing the actual touching of the spheres:

$$\mathbf{F}_{ij}^{lub} = \min\left\{-6\pi\mu\left(\frac{a_i a_j}{a_i + a_j}\right)^2\left(\frac{1}{s} - \frac{1}{\Delta_c}\right), 0\right\} \cdot \mathbf{v}_{\mathbf{n_{ij}}}\,, \tag{18}$$

where, a_i and a_j are the sphere radii, $\mathbf{v}_{\mathbf{n_{ij}}}$ is the normal component of the relative velocity, s is the distance between surfaces, and Δ_c is a cut-off value that controls the extent of short range interaction: for $s > \Delta_c$, $\mathbf{F}_{ij}^{lub} = 0$, and the spheres are subject only to hydrodynamic forces. Ladd and Verberg [38] demonstrated good agreement of the proposed lubrication force with Brenner's exact solution [7].

Equation (18) provides a basic model for the estimation of the lubrication force in normal direction. The calculation of the partial lubrication force between non-spherical surfaces follows the approach proposed in [16] for a LBM formulation yet it is amended to fit the Lagrangian formulation adopted

herein. Accordingly, the force model provided in Eq. (18) is modified as

$$\begin{aligned} \mathbf{F}_{ij}^{lub} &= \sum_k \mathbf{f}_{ij}^k, \\ \text{with } \mathbf{f}_{ij}^k &= \min\left\{-\frac{3}{2}\pi\mu h^2\left(\frac{1}{s^*}-\frac{1}{\Delta_c}\right), 0\right\}\cdot \mathbf{v}_{\mathbf{n_{ij}}}^* \ , \end{aligned} \tag{19}$$

where s^* and $\mathbf{v}_{\mathbf{n_{ij}}}^*$ denote the markers' relative distance and velocity, respectively, and the summation is over all interacting markers of the two solid objects.

2.5. Simulation algorithm

The time evolution of the system is calculated using a second order explicit Runge-Kutta method [3]. At the beginning of each time step, a neighbor list is assembled to indicate the set of markers that fall within the kernel support of each marker; if N markers are used in the simulation, N lists are generated. The force components appearing on the right hand side of Eqs. (4), (5), and (19) are subsequently computed based on these neighbor lists. Two different functions are called to capture the interaction between markers according to their types, i.e., fluid or solid, via SPH or the short range interaction model described in section 2.4. In the second stage, the state of the fluid markers, including position, velocity, and density, is updated based on Eqs. (4), (5), and (8). The state of each rigid body is updated according to Eqs. (12) through (15). Since a rigid wall boundary is a particular instance of a rigid body (with zero or other pre-defined velocity), it requires no special treatment.

The above algorithm was implemented to execute in parallel on Graphics Processing Unit (GPU) cards using Compute Unified Device Architecture

(CUDA) [52]. The hardware used to run the simulations that produced the results reported in this contribution, NVIDIA Kepler K20X, has 2688 parallel scalar processors. At each time step, four different tasks are executed on the GPU to (1) calculate the inter-marker forces, (2) carry out fluid time integration, (3) carry out rigid body time integration, and (4) enforce boundary conditions. The lists of neighbors needed to evaluate the inter-marker forces are generated via a proximity computation algorithm based on a decomposition of the computation domain into cubic bins. The side length of each bin is roughly equal to the size of the support domain of an SPH marker. A hash table is used to sort the markers according to their location in the domain. Based on the sorted hash table, each marker accesses the list of markers intersecting the self and neighboring bins to calculate the forcing terms. The proximity computation algorithm uses the parallel sorting and scan algorithms provided by the Thrust library [27].

To improve the code vectorization through coalesced memory access and use of fast memory (L1/L2 cache, shared memory, and registers), each computation task was implemented as a sequence of light-weight GPU kernels. For instance, different computation kernels are implemented to update the attributes of the rigid bodies, including force, moment, rotation, translation, linear and angular velocity, and location of the BCE markers. A similar coding style was maintained for the density re-initialization, boundary condition implementation, and mapping of the markers' data on an Eulerian grid for post processing.

Table 1: Flow parameters used for the validation of transient Poiseuille flow

density	1000 kg/m^3
viscosity	0.001 N s/m^2
volumetric force, x-direction	0.005 N/m^3
channel width	0.002 m

3. Simulation tool validation

The purpose of this section is to validate the predictive attributes of the SPH-enabled Lagrangian-Lagrangian framework and the correctness of its software implementation. To the best of our knowledge, except for the transient Poiseuille flow in Sect. 3.1, the validation tests discussed next have not been considered in the context of a Lagrangian-Lagrangian formulation via SPH.

3.1. Transient Poiseuille flow

SPH was used in [49] to numerically simulate transient Poiseuille flow at low Reynolds numbers for which an analytical solution is readily available. Although essentially a 2D problem, for validation purposes, the transient Poiseuille flow is simulated using a 3D setup: the 2D flow was generated using periodic boundary conditions on the channel side walls, i.e., in the direction perpendicular to x and y, see Figure 3. For the set of parameters provided in Table 1, results show a virtually exact match between the velocity profiles obtained from the numerical simulation and the analytical solution reported in [49].

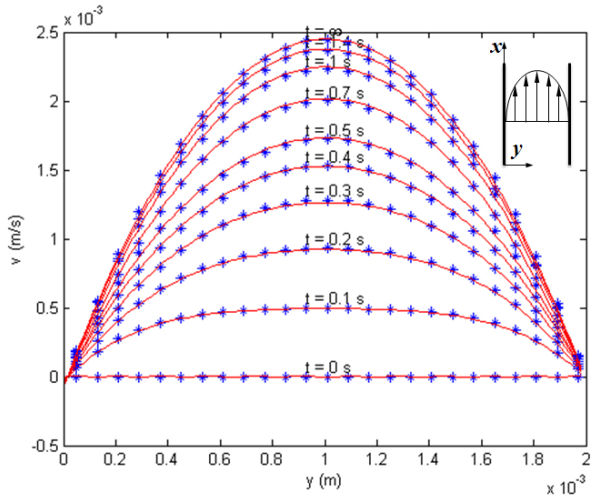

Figure 3: Velocity profile of transient Poiseuille flow obtained from simulation (dots) and series solution (continuous lines) at different times. A schematic of the flow is shown in the top-right corner of the figure to illustrate how the y coordinate is defined.

3.2. Particle migration in 2D Poiseuille flow

Although Segre and Silberberg considered particle migration in pipe flow [64, 65], a similar phenomenon occurs in plane Poiseuille flow. Maintaining the setup of Sect. 3.1, infinitely long cylinders were added into the flow. For a cylinder size $a/w = 0.125$ and $Re_c = 12.73$, where a, w, and Re_c are the cylinder radius, channel width, and channel Reynolds number, respectively, we obtained the same stable lateral positions of the immersed bodies as those reported in [31, 55], with a maximum 1% relative drift with respect to the channel half width as reported in Table 2. Figure 4 shows the trajectories of cylinders released from different initial lateral positions, y, versus non-dimensional time, $t^* = t \times V/L$, where V denotes the mean flow velocity.

Table 2: Stable lateral position at $Re_c = 12.73$ and $a/w = 0.125$

	Re_c	y_c
LBM [31]	12.73	0.2745
DLM/FDM [55]	12.78	0.2732
LL approach	12.75	0.2785, 0.7215

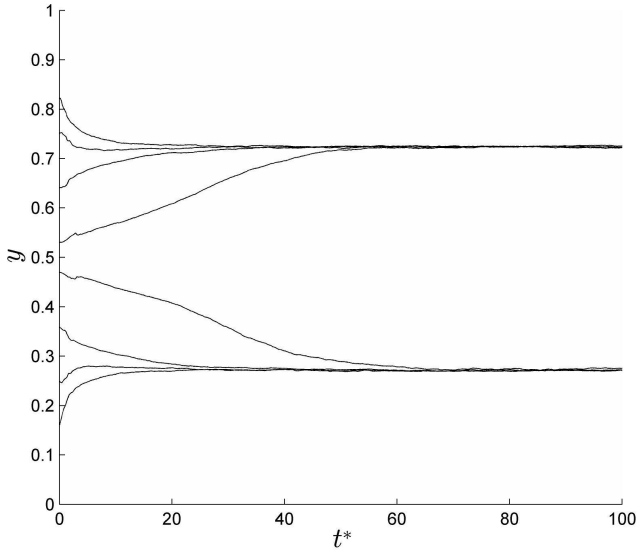

Figure 4: Lateral migration of neutrally buoyant circular cylinder in plane Poiseuille flow at $Re_c = 12.73$ and $a/w = 0.125$. Each line shows the lateral position of a cylinder, released from a specific lateral location, as a function of dimensionless time. The lateral positions are normalized by the channel width, w. Results are within 1% of those reported in [31, 55].

3.3. Particle migration in pipe flow

The experiment conducted by Segre and Silberberg on the motion of a sphere in pipe flow demonstrated a final particle stable radial position of

$r/R \approx 0.6$, where r and R denote the particle offset from the pipe axis and the pipe radius, respectively [64, 65]. The same results are obtained through simulation at $Re \approx 60$, consistent with [64], and particle relative size $a/R = 0.1$, where a denotes the sphere radius (Figure 5). The effects of the Reynolds number and particle size are investigated independently and reported in sub-sections 3.5 and 4.5, respectively.

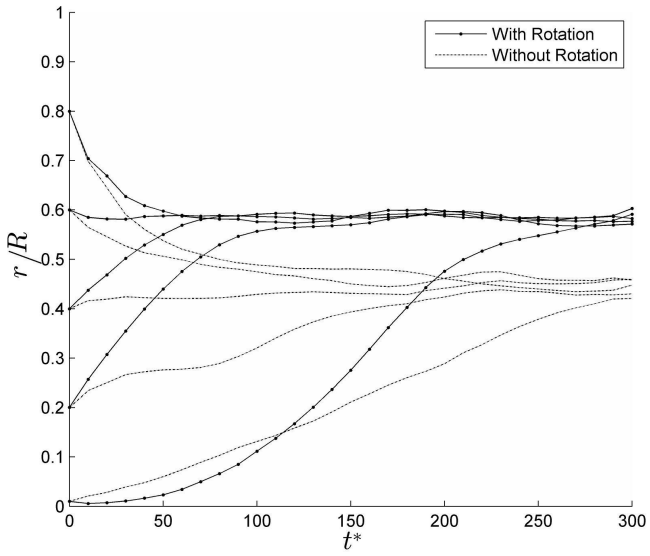

Figure 5: Radial migration of rotating and non-rotating neutrally buoyant spheres in pipe flow at $Re \approx 60$ and $a/R = 0.1$. Each line shows the radial position of a sphere, released at a specific radial position, as a function of dimensionless time. The radial positions are normalized by the pipe radius, R.

3.4. Radial distribution of particles in suspension

This test validates the transient behavior of a suspension of several spheres in pipe flow. The simulation parameters are those in Segre and Silberberg's

experiment [64, 65], which is provided in Table 3. Figure 6 shows a comparison of the particle radial distribution at $Re \approx 60$ with experimental results reported in [64]. Here, $L = (a/R)(av\rho/\mu)(l/R)$ is the non-dimensional distance from the pipe inlet and $v = (a/R)^2 V$ is defined based on mean flow velocity V, sphere radius a, and pipe radius R. The experimental setup considered by Segre and Silberberg [64], i.e., including particle distribution in the range of 1 through 4 particles/cm^3 or volumetric concentration of $\phi \in [0.027, 0.109]\,\%$, is very dilute. As such, generating smooth distribution curves requires a very long channel to include a sufficiently large number of rigid bodies. Reproducing this experiment through simulation requires the flow field to be resolved at a scale fine enough to capture the dynamics of the small rigid bodies suspended in the flow. This translates into a large number of SPH markers. Consequently, the amount of time required to complete a simulation, even when leveraging high performance parallel computing, was prohibitively large. We addressed this issue by performing an ensemble average over a set of smaller channels instead of one single, long channel. Each small channel was subjected to periodic boundary conditions along the channel axis and included between 1 and 16 rigid particles, initialized randomly and tracked independently. In a Monte Carlo framework, a large number of simulations were considered to produce a converged statistical distribution. Yet, this was not an issue as we were able to carry out batches of up to 56 simultaneous simulations (one simulation per GPU card) on the computer cluster available for this study [62]. The distributions reported in Figure 6 are the result of a statistical investigation based on 192 ten-hour-long simulations that capture 14 seconds of real time. The simulation results accurately

Table 3: Parameters used in the simulation of transient behavior of a suspension of particles

sphere's radius	0.4 mm
pipe's radius	5.6 mm
density	1180 kg/m^3
viscosity	0.05 N s/m^2
Reynolds number	60

reproduce (1) the stable radial position, and (2) the longitudinal transition distance observed in experimental tests [64].

To generate the distribution curves, the data was sampled at sections located at predefined distances from the pipe entrance. A very fine radial grid was considered to record the particles' radial positions, which resulted in a noisy output. Subsequently, statistical bootstrapping was used to find the confidence zone and distribution curve [18]. The error bars reported with the distribution curves are associated with the 95% confidence interval.

3.5. Effect of Reynolds number

Matas *et al.* [42] extended the Segre-Silberberg experiment up to $Re \approx 2400$ and demonstrated that the stable radial positions migrate towards the wall as Re increases. However, a second stable region, i.e. an inner annulus, forms at high Re, e.g. $Re > 650$, for $\lambda = a/R \in [0.06, 0.11]$. Moreover, the radial distribution of the particles shifts toward the inner annulus as Re increases. Shao *et al.* [66] numerically confirmed the formation of an inner annulus at high Re via the direct-forcing fictitious domain method [74]. Figure 7 reports over a wide range of Reynolds numbers results obtained with the proposed approach, experimental results presented in [42], and numerical

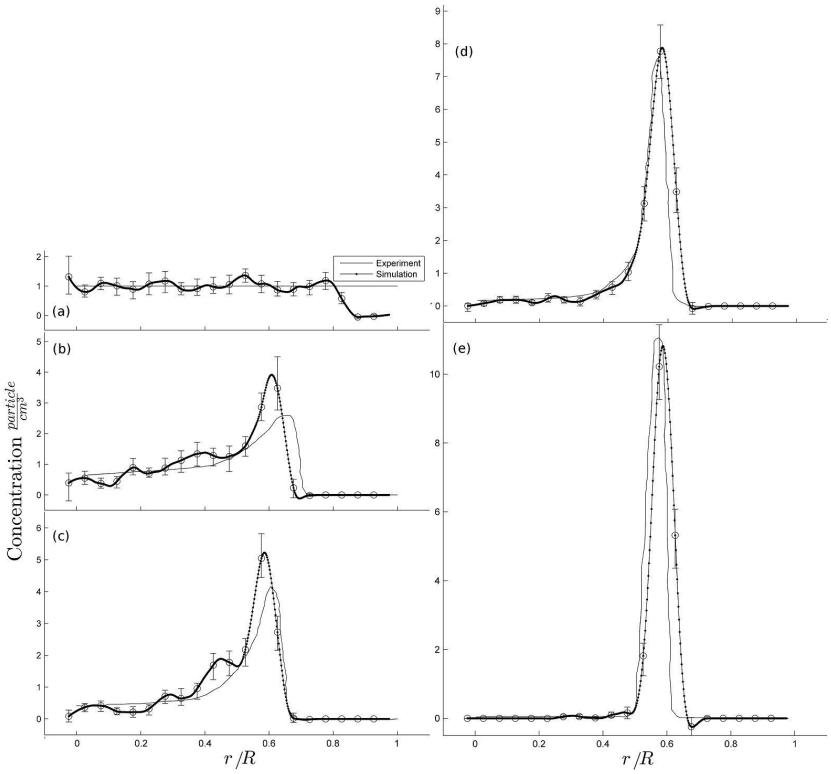

Figure 6: Particle radial distribution as a function of non-dimensional distance, L, from the pipe inlet. Each plot shows the particle distribution as a function of radial distance from channel axis. The simulation results are compared to the experiment [64] at: (a) $L = 0$, (b) $L = 0.08$, (c) $L = 0.16$, (d) $L = 0.32$, (e) $L = 0.69$. Note that rigid bodies cannot be initialized in the region close to the wall, i.e., $0.9 \leq r/R \leq 1$, due to their finite size.

results from [66, 72]. Our numerical results confirm the emergence at higher Reynolds numbers, i.e., $Re \approx 772$ when $\lambda = 0.11$ and $Re \approx 1127$ when $\lambda = 0.15$, of a secondary stable annulus in agreement with [42, 66]. We noticed small differences at $Re > 1200$ from results reported in [66]. However, as Matas *et al.* pointed out in their experimental work, particles tend to appear between the two stable annuli effectively everywhere yet with a higher

probability around the interior annulus.

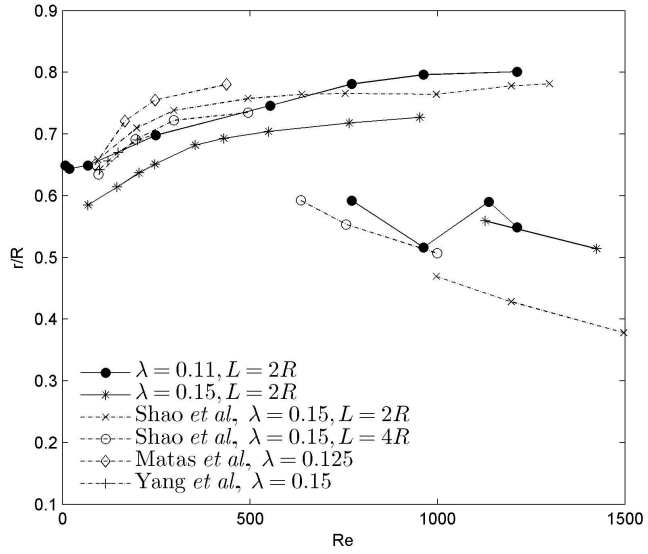

Figure 7: Effect of Re on the tubular pinch effect for $Re \in [1, 1400]$ and two particle size ratios, $\lambda = 0.11$ and $\lambda = 0.15$. Each line shows the dependence of the normalized stable radial position on the Reynolds number for a particular scenario. The results are compared to data provided by Matas *et al.* [42], Yang *et al.* [72], and Shao *et al.* [66].

4. Results and discussion

Unlike the previous section, which focused on validating the proposed approach and its software implementation, this section presents results of several simulations carried out to characterize through direct numerical simulation the effect of particle properties on the radial distribution of suspensions in pipe flow.

4.1. Effect of particle rotation

To identify the root cause of particle migration and gauge the influence of the Magnus effect, Oliver [53] carried out experiments with inertia asymmetric spheres in which the center of mass was shifted from the sphere's geometric center. He showed that as the particle rotation was reduced, the stable final position of these particles moved toward the pipe's axis. Similar investigations for the motion of a cylinder in Poiseuille flow were performed numerically by Patankar *et al.* [58] and Joseph and Ocando [33] to demonstrate the influence of the cylinder rotation on the steady state configuration in 2D flows. Yu *et al.* [73] simulated the motion of a sphere in pipe flow using the DLM/FDM method and showed a similar trend. Herein, we carried out a similar experiment by suppressing the 3D rotation of spheres and demonstrated results similar to those reported in [53, 73], see Fig. 5. Essentially, the rigid body migration is noticeably altered when body rotation is artificially removed. The conclusion is that the behavior of particles in 3D suspension flows may exhibit large deviations from the actual dynamics when body rotation is ignored. Note that the rotation was eliminated by numerically imposing extremely large moments of inertia for the immersed spheres.

4.2. Effect of particle concentration

The experimental results in [64], used herein for validation purposes, only included particle concentrations in the range 1 through 4 particles/cm^3, i.e. volumetric concentration of $\phi \in [0.027, 0.109]\,\%$. The dynamics of monodisperse particles has been numerically investigated herein for the set of parameters given in Table 3 and concentrations of up to $\phi = 3.488\%$. Figure 8 pro-

vides snapshots of particle distribution and resulting annulus formation down the pipe, for concentrations of 32 and 64 particles/cm^3, i.e. $\phi = 0.872\%$ and $\phi = 1.744\%$, respectively. Normalized concentrations, defined as the ratio of the particle local concentration to the initial concentration, are plotted for different volumetric concentration, $\phi \in [0.109, 3.488]\,\%$, in Figure 9, which suggests low probability of spheres hovering close to the pipe's axis. The particle distribution is, however, more spread in denser flows. This deviation can be traced back to two trends: (1) the interaction between rigid bodies through drafting, kissing, and tumbling prevents the particles from coalescing into a narrow annulus; (2) smaller particle distance at denser regimes slows down the rate of migration toward the stable annulus. This will be investigated further in Sect. 4.3.

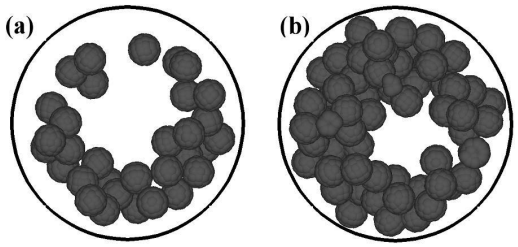

Figure 8: Particle arrangement in the pipe at normalized distance $L = 0.32$. Two different particle concentrations are shown herein: (a) 32 particles/cm^3; (b) 64 particles/cm^3. Tubular pinch effect is observed regardless of the particle concentration. Nevertheless, particles occupy a wider annulus in the denser regime.

4.3. Effect of inter-particle distance

The effect of a particle's wake on the radial migration of trailing particles is investigated using periodic boundary conditions along the channel axis for spheres of radius a, with $a/R = 0.25$, at $Re \approx 60$. The particle initial position

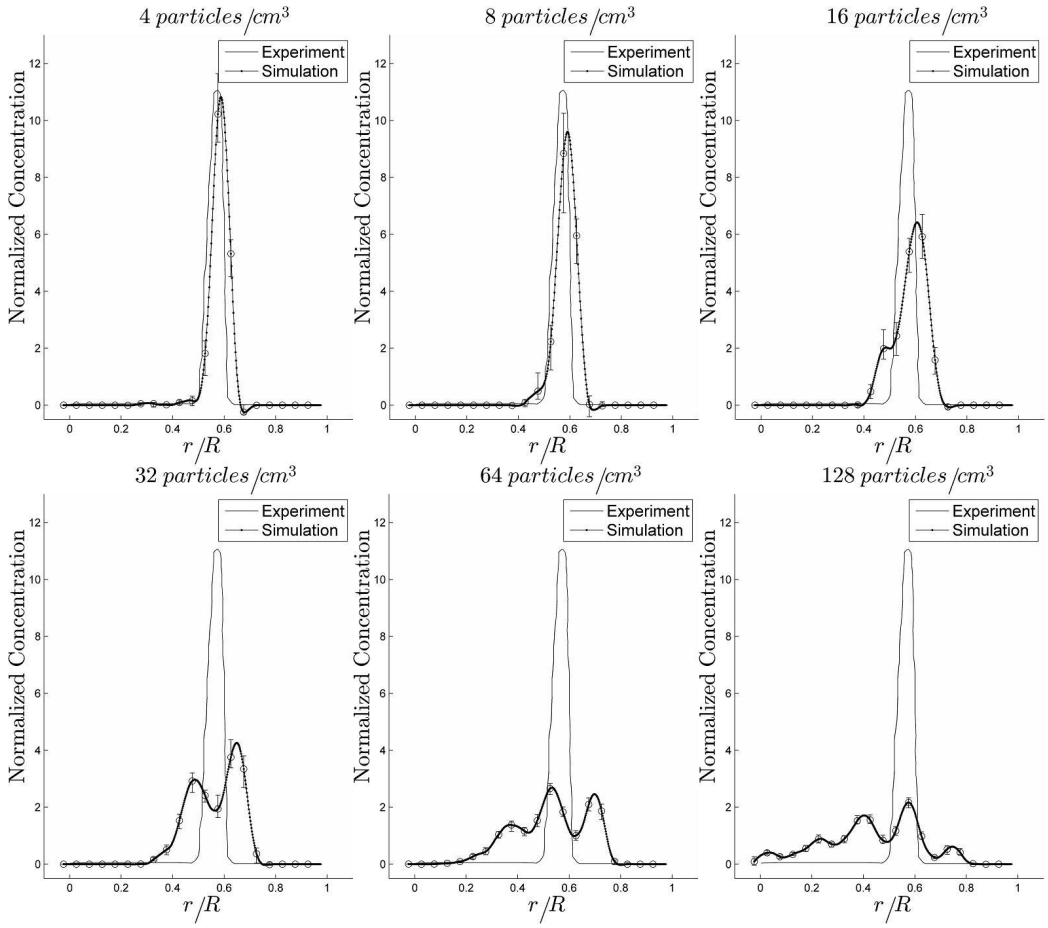

Figure 9: Particle radial distribution at the normalized distance $L = 0.69$, plotted for six different initial concentrations in the range of 4 through 128 particles/cm^3 equivalent to $\phi \in [0.109, 3.488]\,\%$, at $Re \approx 60$. For each scenario, the particle radial distribution is normalized by the initial uniform distribution used for that scenario. Results are compared to a reference experimental distribution reported in [64] at $L = 0.69$ for concentration of 1 particles/cm^3. All scenarios demonstrate the tubular pinch effect, where particles distribution tends to zero close to the channel axis. As expected, the distributions are more spread in denser regimes.

Table 4: Normalized stable radial position, r/R, at $Re \approx 60$, $a/R = 0.25$, and different normalized inter-particle distance, d/a.

d/a	2.50	2.93	3.64	4.28	5.71	7.14	10.00	12.86	14.29
r/R	0.62	0.60	0.58	0.56	0.54	0.52	0.51	0.52	0.52

is close to the pipe axis and inter-particle spacing is adjusted by changing the value d, i.e. the length of one period of the pipe, see Figure 10. The results, reported in Table 4 and Figure 10, suggest that (1) the stable radial position moves closer to the wall as the inter-particle distance decreases, a fact that complies well with [66]; and (2) for very large inter-particle distance, i.e., $d/a \gg 1$, radial migration is independent of inter-particle distance. Finally, Figure 11 indicates that decreasing the inter-particle distance slows down the radial migration, i.e., a particle's wake alters the local flow profile around trailing particles. In other words, while the particles settle further away from the pipe axis, the settling occurs significantly further down the pipe. The result of this test is particularly relevant in the simulation of pipe flow using periodic boundary condition since it suggests a safe value of $d/a > 9$ to avoid the effect caused by the imposition of boundary conditions.

4.4. Effect of particle asymmetry

In most of the experiments and numerical simulations of particle migration, the rigid bodies were spherical and the effect of asymmetry was not discussed. A series of numerical simulations were carried out at $Re \approx 60$ by replacing spheres with ellipsoids of radii (a_1, a_2, a_3), with $a_1 = a_2 = 0.07R$ and $0.07R < a_3 < 0.43R$. The obtained results suggest that, with an increase in skewness, the stable radial particle position moves toward the pipe axis

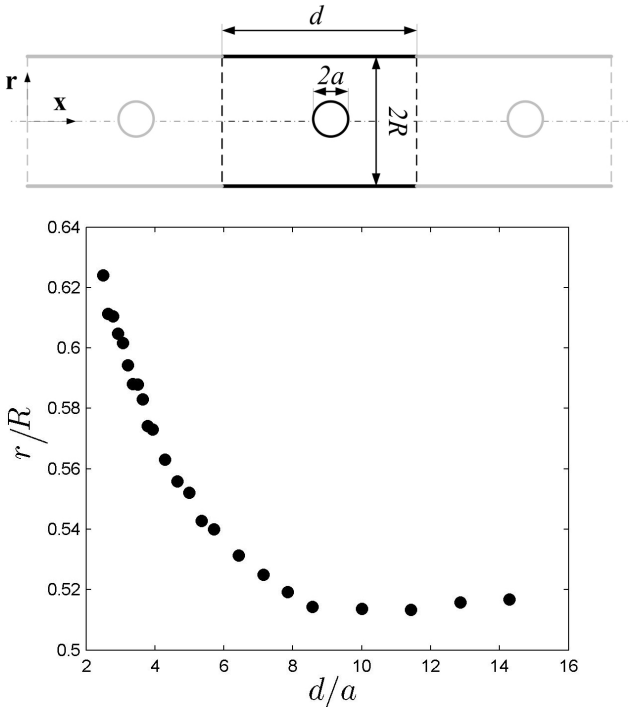

Figure 10: Investigation of the effect of inter-particle distance on the radial migration of particles at $Re \approx 60$ and size ratio $a/R = 0.25$. Top: Schematic of the simulation setup. Periodic boundary is considered in the x-direction; Bottom: Stable radial position of particles as a function of inter-particle distance. The plot shows a decay in the particle migration as the particle distance increases. This result agrees with the findings of Shao *et al.* [66]. Moreover, the particle migration is independent of inter-particle distance when $d/a > 9$.

(Figure 12).

4.5. Effect of particle size

By changing the radius of the neutrally buoyant sphere in the range of $0.07R < a < 0.36R$ at $Re \approx 60$, it is observed that particle radial migration decreases almost linearly as the radius increases (Figure 13).

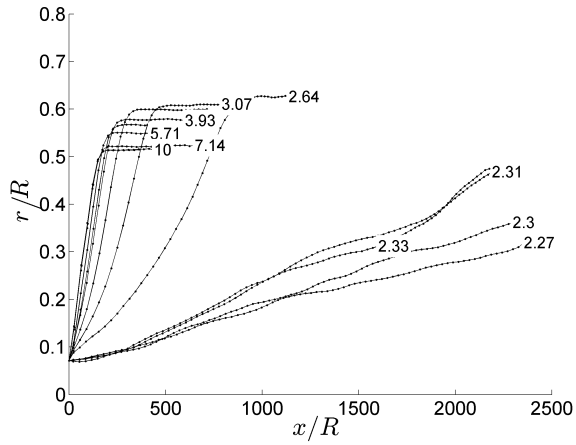

Figure 11: Particle trajectories as a function of a non-dimensional travel distance along the pipe axis x/R, plotted for several inter-particle distances in the range $d/a \in [2.27, 14.3]$, at $Re \approx 60$ and $a/R = 0.25$. The curve labels indicate the value of d/a. To maintain clarity, only some of the curve labels are shown. The results show a decay in the rate of migration as the inter-particle spacing decreases.

4.6. Direct numerical simulation of a dense suspension: a scalability study

As shown in Figure 14a, the simulation times grow linearly with the size of the problem, i.e., the combined number of SPH markers and rigid bodies. A second scaling analysis showed that an increase in the number of rigid bodies present in the system only marginally affects the total simulation time, see Figure 14b. This is due to the fact that changing the rigid body count has a relatively small impact on the total number of discretization markers in the SPH method, which dictates to a very large extent the simulation time. Nevertheless, as the particle concentration increases, smaller time steps are required since the probability of short-range, high-frequency interaction increases. Figure 15 shows a snapshot of a simulation of dense suspension

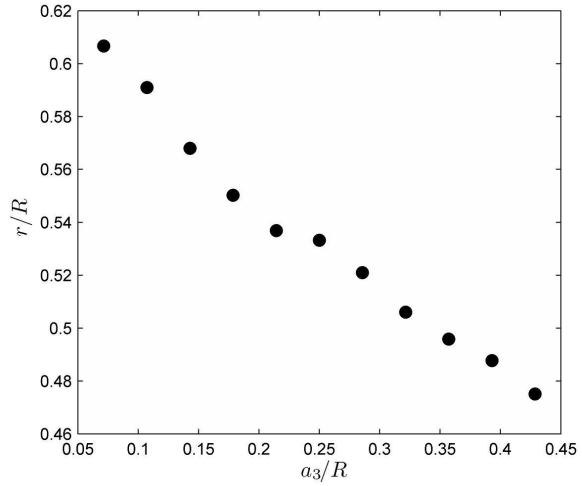

Figure 12: Investigation of the effect of particle skewness on the stable radial position, at $Re \approx 60$. The skewed particles are spheroid of radii $(0.07R, 0.07R, a_3)$ where $a_3 > 0.07R$. For more skewed particles, i.e. larger values of a_3/R, the stable radial position is located closer to the channel axis.

flow, with the properties given in Table 5, taken at about $t^* = 4$. The non-dimensional time is defined as $t^* = t \times V/w$, where w is the channel width.

4.7. Direction of future work: suspensions with moderately low concentration– validation against experimental data

Preliminary 3D results obtained for the simulation of the Poiseuille flow of a suspension with average volumetric fraction $\phi = 6.01\%$, at $Re \approx 66$ confirms the blunting of the velocity profile reported in a 2D numerical study [55] and in experimental works [23, 24, 35, 68], see Figure 16. The concentration distribution curves are noisier than those obtained experimentally by Han *et. al* [24]. Long simulation times (≈ 100 GPU hour per test) prevented

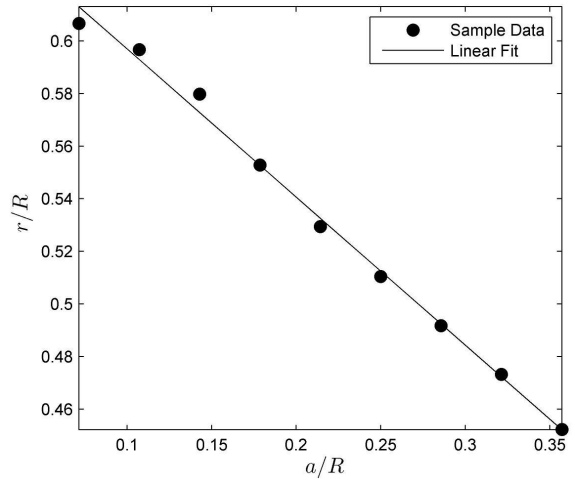

Figure 13: Investigation of the effect of sphere size on the stable radial position, at $Re \approx 60$. Results show a linear dependence of the stable radial position on the particle size. The stable radial position of larger particles is closer to the pipe axis.

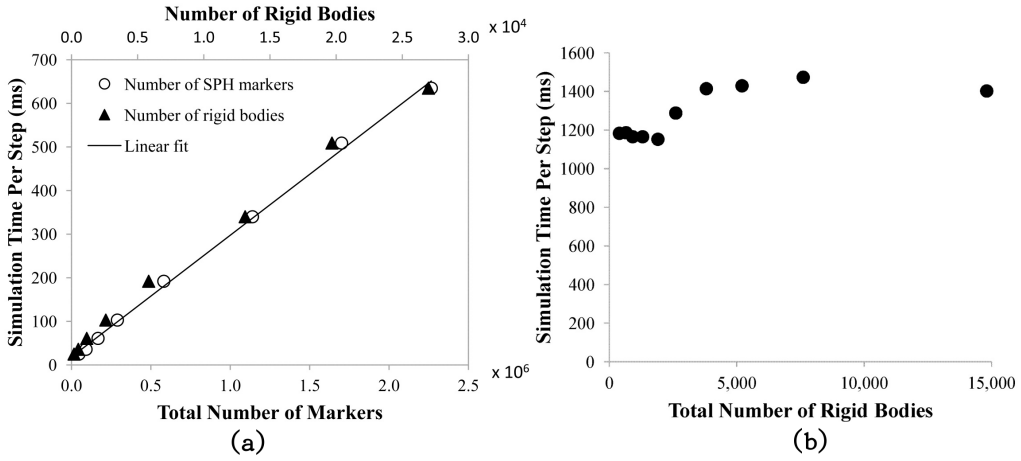

Figure 14: Scaling analysis of the simulation engine: (a) simulation time as a function of the total number of markers and rigid bodies; (b) simulation time as a function of number of rigid bodies for a fixed number of SPH markers.

Table 5: Characteristics of the dense suspension flow

ellipsoid's radii, normalized by channel width	$(2.0, 1.5, 1.5) \times 10^{-2}$
number of ellipsoids	2.3×10^4
volumetric concentration	39.4%
Reynolds number	66

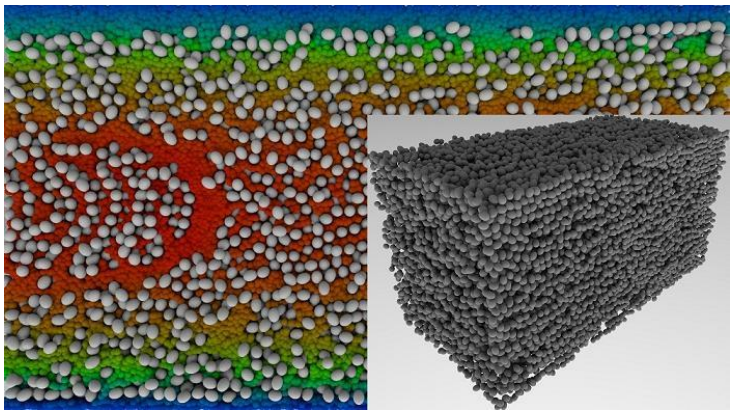

Figure 15: Direct numerical simulation of a dense suspension of ellipsoids in 3D square channel flow with the properties given in Table 5. The mid-section of the flow, which displays the rigid ellipsoids suspended in the fluid, is shown in the background. The color represents fluid velocity: from zero (blue) to maximum (red). The rigid ellipsoids are shown as gray objects. In the inset, the fluid was removed to show a perspective view of the rectangular channel and the dense arrangement of ellipsoids.

us from running a sufficiently large number of simulations required for statistical averaging and bootstrapping. An effort is underway to reduce the simulation times to enable the study of suspensions with moderate to high concentrations.

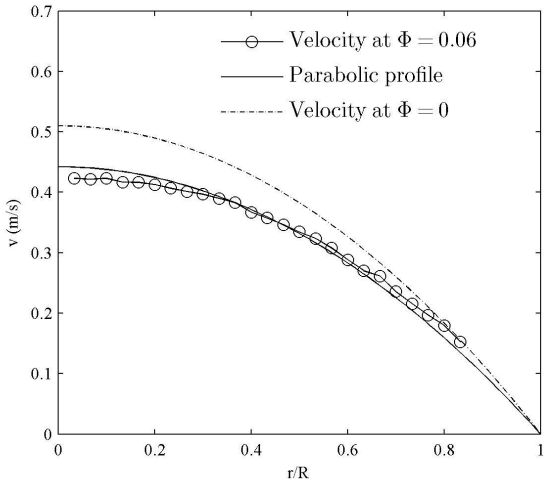

Figure 16: Comparison of the velocity profile of the flow of a suspension, with volumetric fraction $\phi = 6.01\%$, with that of a single phase flow, i.e. $\phi = 0\%$. Results show the blunting of the velocity for the case of a suspension.

5. Conclusions

This contribution introduces a Lagrangian-Lagrangian modeling and simulation framework that is used to characterize dilute and dense particles suspensions. The methodology proposed relies on SPH and 3D rigid body dynamics for the simulation of fluid and solid phases, respectively. A partial lubrication force model for arbitrarily-shaped 3D bodies has been introduced to resolve the solid-solid short range interaction.

Upon validation, the proposed modeling and simulation framework has been used to investigate new phenomena associated with particle suspension dynamics. The outcomes of these studies are summarized as follows:

Influence of particle concentration: investigations were performed on particle suspensions at volumetric concentrations $\phi < 3.5\%$. The simulation

results demonstrate the significant effect of the particle concentration on radial migration even at dilute regimes due to the hydrodynamic and/or short range interaction of particles. Nevertheless, the probability of finding a particle close to the pipe axis remained small in all of the considered scenarios.

Effect of particle distance: the effect of particles hydrodynamic interaction on their radial migration was investigated through the simulation of a line of non-coloidal particles in Poiseuille flow. We found that: (1) the stable radial position moves closer to the wall as the inter-particle distance decreases; (2) for very large inter-particle distance, radial migration is independent of inter-particle distance. More specifically, for the size ratio $a/R = 0.25$ and $Re \approx 60$, the stable radial position remains at $r/R = 0.52$ for $d/a > 9$; (3) decreasing the inter-particle distance slows down the radial migration.

Effect of inter-particle size, shape, and rotation. We found that increasing the particle size linearly decreases the radial migration. Moreover, as the particle skewness increases, i.e. by adopting ellipsoidal particles of variable radii, the radial migration decreases. Finally, by reducing the particle rotation through increasing the mass moment of inertia, the radial migration was found to be reduced, but not eliminated. This test demonstrated the combined effect of particle rotation and flow velocity profile on radial migration.

Through the use of parallel computing we have addressed both long simulation times and scaling in terms of number of particles in suspension. To demonstrate this, we carried out a scaling analysis for dense suspensions of up to $23,000$ ellipsoids at 39.4% volumetric fraction. These analyses were performed on a personal computer and in reasonable amounts of time. The

modeling and simulation times for fluid and rigid body dynamics, fluid-solid interaction, and solid-solid short range interaction are independent of the particle shape. As such, different particle shapes can be selected at no or very little additional cost.

It is worth mentioning that a clogging analysis shares similar physics with the dense suspension modeled in this work: (*i*) particles have geometry/shape and finite size; (*ii*) they actively interact with the fluid, therefore influence the fluid passage; and (*iii*) their interpenetration is removed by implementing an impact model. A successful simulation of the dense suspension with 39.4% particle volumetric fraction, which was carried on in this work, demonstrates that the modeling, numerical, and computational infrastructure required for the clogging formation is in place. Nevertheless, frequent occurrence of rigid body impact may demand an smaller integration time step.

The simulation framework that implements the proposed Lagrangian-Lagrangian approach is available as open source software and can be downloaded at [10].

6. Acknowledgement

The authors would like to thank Dr. Radu Serban for his comments on a draft of this manuscript. Financial support for the first author was provided in part by National Science Foundation, through grant NSF CMMI-084044. The second author was supported through Army Research Office grants W911NF-11-1-0327 and W911NF-12-1-0395. Nvidia is acknowledged for providing the GPU hardware used in generating the simulation results reported herein.

References

[1] Anitescu, M., and Hart, G. D. A constraint-stabilized time-stepping approach for rigid multibody dynamics with joints, contact and friction. *International Journal for Numerical Methods in Engineering 60*, 14 (2004), 2335–2371.

[2] Asmolov, E. S. The inertial lift on a spherical particle in a plane Poiseuille flow at large channel Reynolds number. *Journal of Fluid Mechanics 381* (1999), 63–87.

[3] Atkinson, K. *An introduction to numerical analysis*. John Wiley and Sons, USA, 1989.

[4] Basa, M., Quinlan, N., and Lastiwka, M. Robustness and accuracy of SPH formulations for viscous flow. *International Journal for Numerical Methods in Fluids 60*, 10 (2009), 1127–1148.

[5] Batchelor, G. *An introduction to fluid mechanics*. Cambridge University Press, 1974.

[6] Benz, W. Smoothed particle hydrodynamics: A review. In *Proceedings of the NATO Advanced Research Workshop on The Numerical Modelling of Nonlinear Stellar Pulsations Problems and Prospects, Les Arcs, France, March 20-24* (1986), Kluwer Academic Publishers.

[7] Brenner, H. The slow motion of a sphere through a viscous fluid towards a plane surface. *Chemical Engineering Science 16*, 3 (1961), 242–251.

[8] Chen, S., Pan, T., and Chang, C. The motion of a single and multiple neutrally buoyant elliptical cylinders in plane Poiseuille flow. *Physics of Fluids 24* (2012), 103 302.

[9] Choi, H. G., and Joseph, D. D. Fluidization by lift of 300 circular particles in plane Poiseuille flow by direct numerical simulation. *Journal of Fluid Mechanics 438*, 1 (2001), 101–128.

[10] Chrono::Fluid. An Open Source Engine for Fluid-Solid Interaction. `http://armanpazouki.github.io/chrono-fluid/`, 2014.

[11] Chun, B., and Ladd, A. Inertial migration of neutrally buoyant particles in a square duct: An investigation of multiple equilibrium positions. *Physics of Fluids 18* (2006), 031 704.

[12] Colagrossi, A., and Landrini, M. Numerical simulation of interfacial flows by smoothed particle hydrodynamics. *Journal of Computational Physics 191*, 2 (2003), 448–475.

[13] Cole, R. H. Underwater explosions. *Physics Today 1*, 6 (2009), 35–35.

[14] Davis, R. H., Serayssol, J.-M., and Hinch, E. Elastohydrodynamic collision of two spheres. *Journal of Fluid Mechanics 163* (1986), 479–97.

[15] Dilts, G. Moving-least-squares-particle hydrodynamics–I. consistency and stability. *International Journal for Numerical Methods in Engineering 44*, 8 (1999), 1115–1155.

[16] Ding, E.-J., and Aidun, C. K. Extension of the lattice-Boltzmann method for direct simulation of suspended particles near contact. *Journal of Statistical Physics 112*, 3-4 (2003), 685–708.

[17] Durlofsky, L., Brady, J. F., and Bossis, G. Dynamic simulation of hydrodynamically interacting particles. *Journal of Fluid Mechanics 180*, 1 (1987), 21–49.

[18] Efron, B., and Tibshirani, R. *An introduction to the bootstrap*. Chapman and Hall/CRC press, 1993.

[19] Feng, J., Hu, H., and Joseph, D. Direct simulation of initial value problems for the motion of solid bodies in a Newtonian fluid Part 1. sedimentation. *Journal of Fluid Mechanics 261* (1994), 95–134.

[20] Feng, Z., and Michaelides, E. The immersed boundary-lattice Boltzmann method for solving fluid–particles interaction problems. *Journal of Computational Physics 195*, 2 (2004), 602–628.

[21] Gingold, R. A., and Monaghan, J. J. Smoothed particle hydrodynamics-theory and application to non-spherical stars. *Monthly Notices of the Royal Astronomical Society 181*, 1 (1977), 375–389.

[22] Glowinski, R., Pan, T., Hesla, T., and Joseph, D. A distributed Lagrange multiplier/fictitious domain method for particulate flows. *International Journal of Multiphase Flow 25*, 5 (1999), 755–794.

[23] Hampton, R., Mammoli, A., Graham, A., Tetlow, N., and Altobelli, S. Migration of particles undergoing pressure-driven flow in a circular conduit. *Journal of Rheology 41* (1997), 621–640.

[24] Han, M., Kim, C., Kim, M., and Lee, S. Particle migration in tube flow of suspensions. *Journal of Rheology 43* (1999), 1157–1174.

[25] Haug, E. *Computer aided kinematics and dynamics of mechanical systems*. Allyn and Bacon Boston, 1989.

[26] Ho, B., and Leal, L. Inertial migration of rigid spheres in two-dimensional unidirectional flows. *Journal of Fluid Mechanics 65*, 02 (1974), 365–400.

[27] Hoberock, J., and Bell, N. Thrust: C++ template library for CUDA. `http://thrust.github.com/`.

[28] Hogg, A. J. The inertial migration of non-neutrally buoyant spherical particles in two-dimensional shear flows. *Journal of Fluid Mechanics 272* (1994), 285–318.

[29] Hu, H., Patankar, N., and Zhu, M. Direct numerical simulations of fluid-solid systems using the arbitrary Lagrangian-Eulerian technique. *Journal of Computational Physics 169*, 2 (2001), 427–462.

[30] Hu, H. H. Direct simulation of flows of solid-liquid mixtures. *International Journal of Multiphase Flow 22*, 2 (1996), 335–352.

[31] Inamuro, T., Maeba, K., and Ogino, F. Flow between parallel walls containing the lines of neutrally buoyant circular cylinders. *International Journal of Multiphase Flow 26*, 12 (2000), 1981–2004.

[32] Jeffrey, R. C., and Pearson, J. Particle motion in laminar vertical tube flow. *Journal of Fluid Mechanics 22*, 4 (1965), 721–735.

[33] Joseph, D., Ocando, D., and Huang, P. Slip velocity and lift. *Journal of Fluid Mechanics 454* (2002), 263–286.

[34] Karnis, A., Goldsmith, H., and Mason, S. The flow of suspensions through tubes: V. Inertial effects. *The Canadian Journal of Chemical Engineering 44*, 4 (1966), 181–193.

[35] Koh, C. J., Hookham, P., and Leal, L. An experimental investigation of concentrated suspension flows in a rectangular channel. *Journal of Fluid Mechanics 266*, 1 (1994), 1–32.

[36] Kruggel-Emden, H., Simsek, E., Rickelt, S., Wirtz, S., and Scherer, V. Review and extension of normal force models for the discrete element method. *Powder Technology 171*, 3 (2007), 157–173.

[37] Kruggel-Emden, H., Wirtz, S., and Scherer, V. A study on tangential force laws applicable to the discrete element method (DEM) for materials with viscoelastic or plastic behavior. *Chemical Engineering Science 63*, 6 (2008), 1523–1541.

[38] Ladd, A., and Verberg, R. Lattice-boltzmann simulations of particle-fluid suspensions. *Journal of Statistical Physics 104*, 5-6 (2001), 1191–1251.

[39] Ladd, A. J. Sedimentation of homogeneous suspensions of non-Brownian spheres. *Physics of Fluids 9* (1997), 491–499.

[40] Liu, M. B., and Liu, G. R. Smoothed particle hydrodynamics (SPH): An overview and recent developments. *Archives of Computational Methods in Engineering 17*, 1 (2010), 25–76.

[41] Lucy, L. B. A numerical approach to the testing of the fission hypothesis. *The Astronomical Journal 82* (1977), 1013–1024.

[42] Matas, J.-P., Morris, J. F., and Guazzelli, E. Inertial migration of rigid spherical particles in Poiseuille flow. *Journal of Fluid Mechanics 515*, 1 (2004), 171–195.

[43] Matas, J.-P., Morris, J. F., and Guazzelli, E. Lateral force on a rigid sphere in large-inertia laminar pipe flow. *Journal of Fluid Mechanics 621* (2009), 59–67.

[44] Monaghan, J. J. An introduction to SPH. *Computer Physics Communications 48*, 1 (1988), 89–96.

[45] Monaghan, J. J. On the problem of penetration in particle methods. *Journal of Computational Physics 82*, 1 (1989), 1–15.

[46] Monaghan, J. J. Smoothed particle hydrodynamics. *Annual Review of Astronomy and Astrophysics. 30* (1992), 543–574.

[47] Monaghan, J. J. Smoothed particle hydrodynamics. *Reports on Progress in Physics 68*, 1 (2005), 1703–1759.

[48] Monaghan, J. J., and Lattanzio, J. C. A refined particle method for astrophysical problems. *Astronomy and astrophysics 149* (1985), 135–143.

[49] Morris, J., Fox, P., and Zhu, Y. Modeling low Reynolds number incompressible flows using SPH. *Journal of Computational Physics 136*, 1 (1997), 214–226.

[50] Morris, J. P. *Analysis of smoothed particle hydrodynamics with applications*. Monash University Australia, 1996.

[51] Morris, J. P. A study of the stability properties of smooth particle hydrodynamics. *Proceedings of the Astronomical Society of Australia 13*, 1 (1996), 97–102.

[52] NVIDIA. CUDA developer zone. `https://developer.nvidia.com/cuda-downloads`, 2014.

[53] Oliver, D. Influence of particle rotation on radial migration in the Poiseuille flow of suspensions. *Nature 194* (1962), 1269–1271.

[54] Pan, T., Chang, C., and Glowinski, R. On the motion of a neutrally buoyant ellipsoid in a three-dimensional Poiseuille flow. *Computer Methods in Applied Mechanics and Engineering 197*, 25 (2008), 2198–2209.

[55] Pan, T., and Glowinski, R. Direct simulation of the motion of neutrally buoyant circular cylinders in plane Poiseuille flow. *Journal of Computational Physics 181*, 1 (2002), 260–279.

[56] Pan, T.-W. Numerical simulation of the motion of neutrally buoyant particles in the plane Poiseuille flow of a Newtonian fluid. *Comptes Rendus de l'Académie des Sciences-Series IIB-Mechanics 329*, 6 (2001), 435–438.

[57] Pan, T.-W., and Glowinski, R. Direct simulation of the motion of neutrally buoyant balls in a three-dimensional poiseuille flow. *Comptes Rendus Mécanique 333*, 12 (2005), 884–895.

[58] Patankar, N., Huang, P., Ko, T., and Joseph, D. Lift-off of a single particle in Newtonian and viscoelastic fluids by direct numerical simulation. *Journal of Fluid Mechanics 438* (2001), 67–100.

[59] Patankar, N., Ko, T., Choi, H., and Joseph, D. A correlation for the lift-off of many particles in plane Poiseuille flows of Newtonian fluids. *Journal of Fluid Mechanics 445* (2001), 55–76.

[60] Pazouki, A., and Negrut, D. Direct simulation of lateral migration of buoyant particles in channel flow using GPU computing. In *Proceedings of the 32nd Computers and Information in Engineering Conference, CIE32, August 12-15, Chicago, IL, USA* (2012), American Society of Mechanical Engineers.

[61] Saffman, P. The lift on a small sphere in a slow shear flow. *Journal of Fluid Mechanics 22*, 02 (1965), 385–400.

[62] SBEL. Simulation Based Engineering Laboratory, University of Wisconsin-Madison. `http://sbel.wisc.edu`, 2014.

[63] Schonberg, J., and Hinch, E. Inertial migration of a sphere in Poiseuille flow. *Journal of Fluid Mechanics 203*, 1 (1989), 517–524.

[64] Segre, G., and Silberberg, A. Radial particle displacements in Poiseuille flow of suspensions. *Nature 189* (1961), 209–210.

[65] Segre, G., and Silberberg, A. Behaviour of macroscopic rigid spheres in Poiseuille flow Part 1. determination of local concentration by statistical analysis of particle passages through crossed light beams. *Journal of Fluid Mechanics 14*, 01 (1962), 115–135.

[66] Shao, X., Yu, Z., and Sun, B. Inertial migration of spherical particles in circular poiseuille flow at moderately high reynolds numbers. *Physics of Fluids 20* (2008), 103 307.

[67] Singh, P., Hesla, T., and Joseph, D. Distributed Lagrange multiplier method for particulate flows with collisions. *International Journal of Multiphase Flow 29*, 3 (2003), 495–509.

[68] Sinton, S. W., and Chow, A. W. NMR flow imaging of fluids and solid suspensions in poiseuille flow. *Journal of Rheology 35* (1991), 735–772.

[69] Swaminathan, T., Mukundakrishnan, K., and Hu, H. Sedimentation of an ellipsoid inside an infinitely long tube at low and intermediate Reynolds numbers. *Journal of Fluid Mechanics 551* (2006), 357–386.

[70] Swegle, J., Attaway, S., Heinstein, M., Mello, F., and Hicks, D. An analysis of smoothed particle hydrodynamics. *NASA STI/Recon Technical Report N 95* (1994), 17439.

[71] Vasseur, P., and Cox, R. The lateral migration of a spherical particle in two-dimensional shear flows. *Journal of Fluid Mechanics 78*, 2 (1976), 385–413.

[72] Yang, B., Wang, J., Joseph, D., Hu, H. H., Pan, T.-W., and Glowinski, R. Migration of a sphere in tube flow. *Journal of Fluid Mechanics 540* (2005), 109–131.

[73] Yu, Z., Phan-Thien, N., and Tanner, R. I. Dynamic simulation of sphere motion in a vertical tube. *Journal of Fluid Mechanics 518* (2004), 61–93.

[74] Yu, Z., and Shao, X. A direct-forcing fictitious domain method for particulate flows. *Journal of Computational Physics 227*, 1 (2007), 292–314.